Multimodal mass spectrometry imaging for plaque- and region-specific neurolipidomics in an Alzheimer's disease mouse model

Timothy J. Trinklein[1,2], Stanislav S. Rubakhin[1,2], Samuel Okyem[1], Seth W. Croslow[1,2], Marisa Asadian[1], K.R. Sabitha[4], Orly Lazarov[4]*, Fan Lam[2,3]*, Jonathan V. Sweedler[1,2,3]*

[1]Department of Chemistry, University of Illinois at Urbana-Champaign, Urbana, Illinois, USA

[2]Beckman Institute for Advanced Science and Technology, University of Illinois at Urbana-Champaign, Urbana, Illinois, USA

[3]Department of Bioengineering, University of Illinois at Urbana-Champaign, Urbana, Illinois, USA

[4]Department of Anatomy and Cell Biology, College of Medicine, The University of Illinois at Chicago

*Correspondence: olazarov@uic.edu (O.L.) , fanlam1@illinois.edu, (F.L.), jsweedle@illinois.edu (J.V.S.)

Abstract

The progressive accumulation of amyloid beta (Aβ) plaques is a hallmark of Alzheimer's disease (AD). However, the biochemical mechanisms of their formation and the consequences associated with plaque formation remain elusive. Changes in lipid compositions have been reported in AD using targeted mass spectrometry approaches and connected to neuroinflammation but provided limited spatial detail. We report here a new non-targeted approach for discovering and mapping region-specific, plaque-associated lipids including isomers. We accomplish this via a multimodal framework that integrates matrix assisted laser desorption/ionization with laser-induced postionization (MALDI-2) mass spectrometry imaging and trapped ion mobility spectrometry-based spatial lipidomics. Our approach integrates significantly enhanced detectability and spatial-chemical resolution, fluorescence microscopy, and a computational pipeline for multimodal image co-registration and untargeted discovery of plaque-altered lipids. Plaque-associated and brain-region-specific lipidomic changes with striking lipid heterogeneity among individual Aβ plaques across different regions were revealed, as well as unique spatial distributions of lipid isomers around Aβ plaques in a mouse AD model. This approach provides a new tool to enhance our understanding of the Aβ microenvironment.

Keywords

Mass spectrometry, Lipids, Alzheimer's disease, ion mobility, multimodal

Introduction

Alzheimer's disease (AD) is the most prevalent form of dementia.[1] The hallmark pathologies of AD include amyloid beta (Aβ) plaque formation and neurofibrillary tangles, which are associated with cell death and brain atrophy.[1,2] Recently, spatial transcriptomic studies have revelaed the rich and complex molecular alterations in the Aβ plaque microenvironment.[3] In concert, there is a rising interest to investigate the connections between brain lipids, which cannot be directly measured from gene expression data, and their relation to the progression of AD pathologies.[4] For example, the most significant genetic risk factor for late-onset Alzheimer's disease is the presence of the E4 allele of apolipoprotein (APOE E4), a lipid transport protein.[5] It has been suggested that APOE4 promotes neuroinflammatory responses,[6] including the formation of reactive astrocytes and activated microglia. Further evidence suggests that cholesterol-rich lipid rafts may be the primary domain in which processing of amyloid precursor protein (APP) takes place.[7] Interestingly, several classes of lipids appear to spatially altered in the vicinity of Aβ plaques. These include gangliosides, an abundant class of glycolipids, and sulfatides, specialized components of myelin sheaths which are decreased early in AD pathogensis.[8] Taken together, these findings highlight a strong link between AD pathology and the lipidome.

Matrix assisted laser desorption/ionization mass spectrometry imaging (MALDI MSI) is a tool of choice for the label-free mapping of hundreds of lipids and other endogenous molecules simultaneously and in situ, offering unmatched spatial-chemical specificity.[9–11] The ability of MALDI to map lipids, as well as Aβ peptides, in rodent models of AD has been demonstrated,[12–20] revealing colocalization of several lipids to Aβ plaques including simple gangliosides, concomitant with the depletion of sulfatides in the same areas. Further, lipid and peptide imaging has been applied to postmortem human AD tissue from both familial[21] and sporadic AD patients,[22–24] demonstrating that many of the same lipid species observed to be spatially altered in animal models are also dysregulated in humans.

Despite progress, the molecular portrait of the lipidome in AD is incomplete due to limited chemical detail, spatial resolution, and brain coverage offered by existing approaches. Particularly, reliance on targeted lipid analysis and manual peak selection inherently limits the obtainable lipid coverage leading to potential biases. Second, previously reported spatial resolutions are insufficient to fully characterize the plaque microenvironment. Third, large brain coverage is necessary to understand global lipid alterations between different key anatomical regions, especially those more susceptible to AD pathology versus less resilient areas. Finally, multiple isomeric forms of lipids are functionally important but non-trivial to characterize, requiring enhanced instrumentation and methods.

Here we present a combined instrumental and computational workflow for unbiased mapping and nontargeted discovery of AD-associated lipids with high sensitivity and molecular specificity, using the 5xFAD mouse model of AD as an evaluation platform.[25,26] Specifically, MALDI with post-ionization (MALDI-2)[27,28] is employed to enhance detectability and facilitate imaging at high-spatial resolutions while maintaining chemical detail. We then introduce a computational pipeline for coregistration of MSI data with Aβ-stained fluorescence images, automatic Aβ-plaque-localized pixel selection in the hyperspectral MS images, and unsupervised clustering of plaque-associated lipid profiles across brain regions. This workflow follows the concepts of our image-guided mass spectrometry approach, microMS[29] used for single cell[10,30] and subcellular measurements.[31] Here, instead of dissociating the tissue, we use optical microscopy to guide the data analysis of MS images, targeting extracellular plaques rather than cells. By comparison

of pixels associated with plaques and control pixels, lipids enriched or depleted within and near Aβ plaques are highlighted. Multimodal acquisition and co-registration also revealed heterogeneity in lipid contents among plaques in different brain regions. Finally, we employ trapped ion mobility spectrometry (TIMS) to resolve lipid isomers exhibiting differential distribution in AD tissue and confirm the structure of the separated isomers by sequential TIMS – collision induced dissociation (CID). This approach enables spatial lipidomic profiling of AD brains with combined high spatial resolution and isomer separation, providing a powerful tool to study biochemistry in the Aβ plaque microenvironment

Results
Non-targeted discovery of plaque-associated lipids
   To probe the lipid landscape within the Aβ plaque microenvironment, we developed a high-spatial-resolution MALDI-2 MSI approach with multimodal data analysis (Fig. 1). Here, the use of 5-μm spatial resolution with excellent detectability,[14] was achieved by leveraging the signal
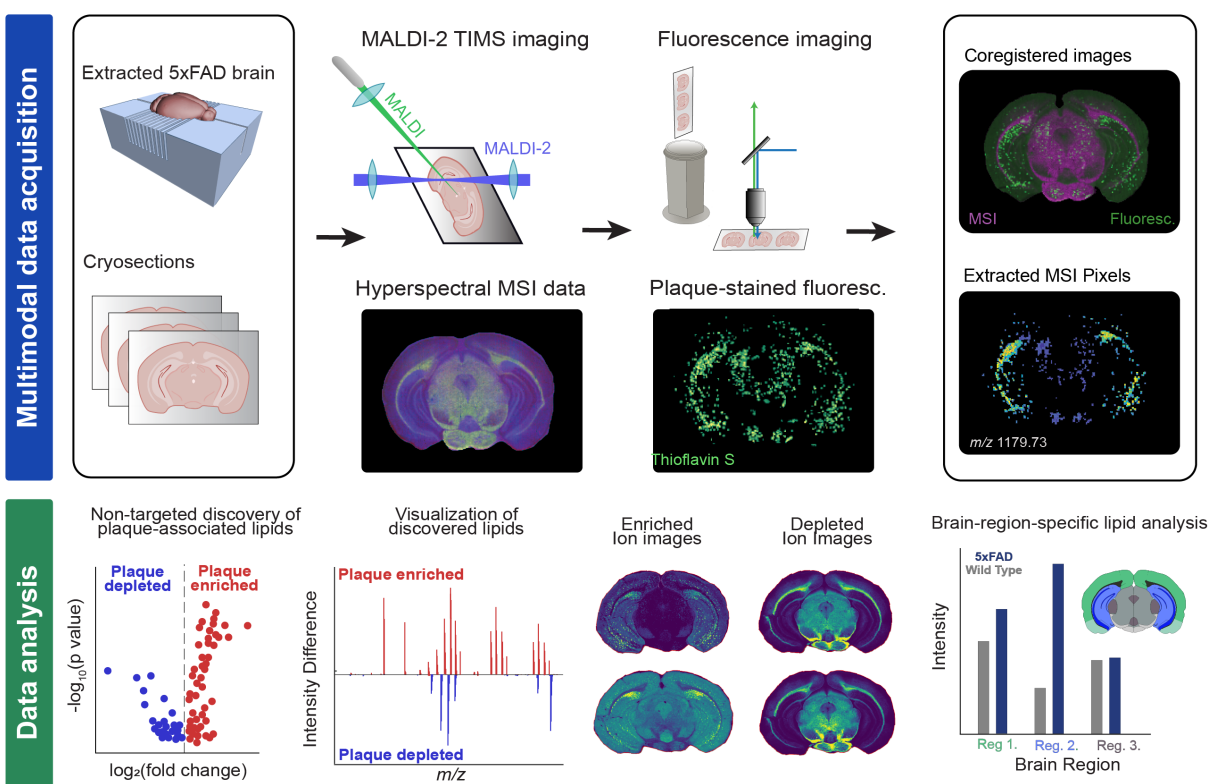

Fig 1. Framework for discovery of plaque-related lipids with multimodal mass spectrometry and fluorescence imaging and computational methods. (Top) Obtained from extracted mouse brain, cryosections are imaged using MALDI-2 TIMS MS, followed by Aβ staining on the same-section and fluorescence imaging. The images are coregistered and plaque-associated pixels and brain regions are automatically extracted from MSI data. (Bottom) Plaque-enriched and depleted lipids are determined from multiple hypothesis testing and visualized by volcano plots and subtraction spectra. Plaque-association is confirmed by inspection of ion images for discovered features. Finally, brain-region-specific lipid alterations with enhanced brain coverage are determined.

enhancement afforded by MALDI-2. A multimodal, computational approach was used to discover plaque-associated and plaque-depleted lipids via accurate coregistration of Thioflavin S-stained fluorescence images and MSI data (details in Fig. S1), non-targeted lipid discovery, and atlas-informed brain region segmentation and lipid analysis (Fig. 1).

Because the utility of MALDI-2 to profile neurodegenerative disease models has not yet been shown, we first evaluated if MALDI-2 could provide signal enhancement for lipids previously shown to be dysregulated in AD. In positive ion mode, significant signal enhancement was obtained for known AD-associated lipids including Vitamin A_1, cholesterol, and *lyso*-phosphatidylcholines (Fig. S2). In negative mode, enhancement of AD-associated phosphatidylethanolamines (PE) and sulfatides (ST) was observed (Fig. S3). In contrast, we observed a decrease in signal of monogangliosides (GM) GM1(36:1) and GM(38:1), which were associated with the generation of asialo-ganglioside (GA1) fragment ions, in agreement with the observations of Soltwisch et al.[27] (Fig. S3). Overall, we found that MALDI-2 enhanced the signal of many low-abundance species in both positive and negative ion modes. Encouraged by the signal enhancement observed in these characterization experiments, we next generated a non-targeted workflow to find plaque-associated lipids using the detection enhancement from MALDI-2. Because a majority of lipid classes known to be implicated in AD are better detected in negative ion mode, we focused on negative mode data for the remainder of this work.

To assess the viability of our multimodal computational approach, we compared fluorescence images to MALDI ion images of lipids previously reported to be plaque localized. Individual Aβ plaques were readily detected by fluorescence imaging following Thioflavin S staining of coronal tissue sections from a 5xFAD mouse brain (Fig. 2a). Comparison of fluorescence images to MSI images of monoganglioside GM3(36:1) (Fig. 2b) a lipid known to accumulate in Aβ plaques,[21,24,32] obtained at 5-μm spatial resolution from the same section *post*-MSI show a high degree of colocalization (Fig. 2c), validating this approach. Additional comparison to a lipid species known to be depleted in Aβ plaques, the sulfatide ST(42:1)[21] provides further confirmation (Fig. 2d-f). In principle, direct imaging of Aβ peptides via MALDI *post*-lipid MSI can be done. However, since peptide imaging on the same section requires tissue rinsing, matrix reapplication, and an additional MSI run, we chose a multimodal MSI and fluorescence approach to facilitate lipid discovery due to higher throughput as well as higher spatial resolution
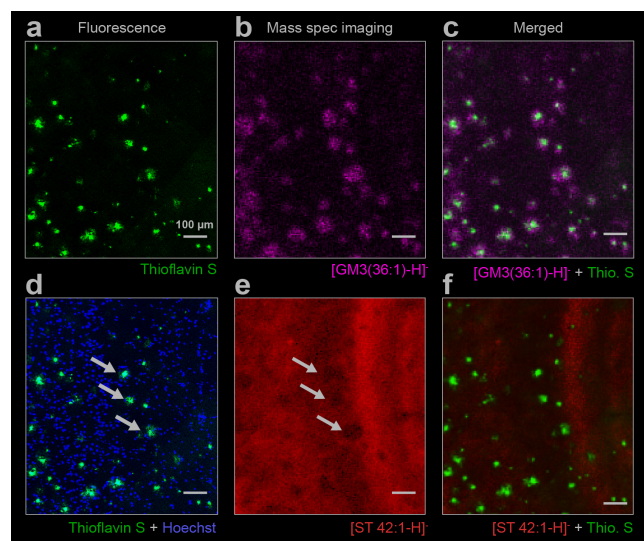

Fig 2. (a) Fluorescence images of tissue stained for Aβ plaques by Thioflavin S *post*-MSI. **(b)** MSI image of the same region shows GM3(36:1), a monoganglioside. **(c)** Merged fluorescence and MSI data show colocalization of GM3(36:1) to Aβ plaques. **(d)**. Thioflavin S and Hoechst highlights cell nuclei size and location relative to plaques, arrows indicate regions of Thioflavin S+ plaques **(e)** MSI image of ST(42:1) shows depletion of sulfatides around Aβ plaques, **(f)** Merged fluorescence and MSI image of ST(42:1) and Thioflavin S.

of Aβ plaques. However, to confirm the specificity of Thioflavin S to Aβ plaques, we compared fluorescence images to direct detection of Aβ$_{1-40}$ and Aβ$_{1-42}$ via MALDI (Supporting Information and Fig. S3) and observed excellent correlation.

Building on these results, we next developed a computational approach to select pixels from Aβ plaques and compare them to control pixels for nontargeted discovery of altered lipids. Briefly, MSI data and fluorescence data (obtained *post*-MSI) were coregistered via affine transformation (Fig. S4). Pixels in the MSI data that aligned with Aβ plaques were extracted (Fig. 3a-b), while an equal number of control pixels were extracted from regions that did not stain for Thioflavin S (Fig. 3c). Specifically, control pixels were selected by first dilating a region of pixels around each plaque within a 200 µm diameter. Any pixels in the plaque-surrounding region that were positive for Thioflavin S, indicative of a nearby plaque, were excluded and replaced with the next-closest Thioflavin S negative pixels to maintain an equal number of pixels in each group.

To avoid redundant features from isotopic peaks as well as matrix and fragment ions, we first refined *m/z* features to a list of putative lipids. To accomplish this, we searched all *m/z* features on LIPIDMAPS[33] for negative ions with a mass tolerance of 0.01 *m/z*. This feature list was further refined by ensuring that each putative lipid also exhibited at least one expected isotopic peak in addition to the monoisotopic *m/z*. Next, we tested each of the refined lipid features for significance to identify putative plaque-associated lipids. A parametric *t*-test was used as a majority (79%) of lipid features were normally distributed ($p>0.05$ via Shapiro Wilk test).

The results are readily visualized in volcano plots (Fig. 3d) and averaged subtraction plots (Fig. 3e). We observed plaque-colocalization of monogangliosides including GM3 and GM2,
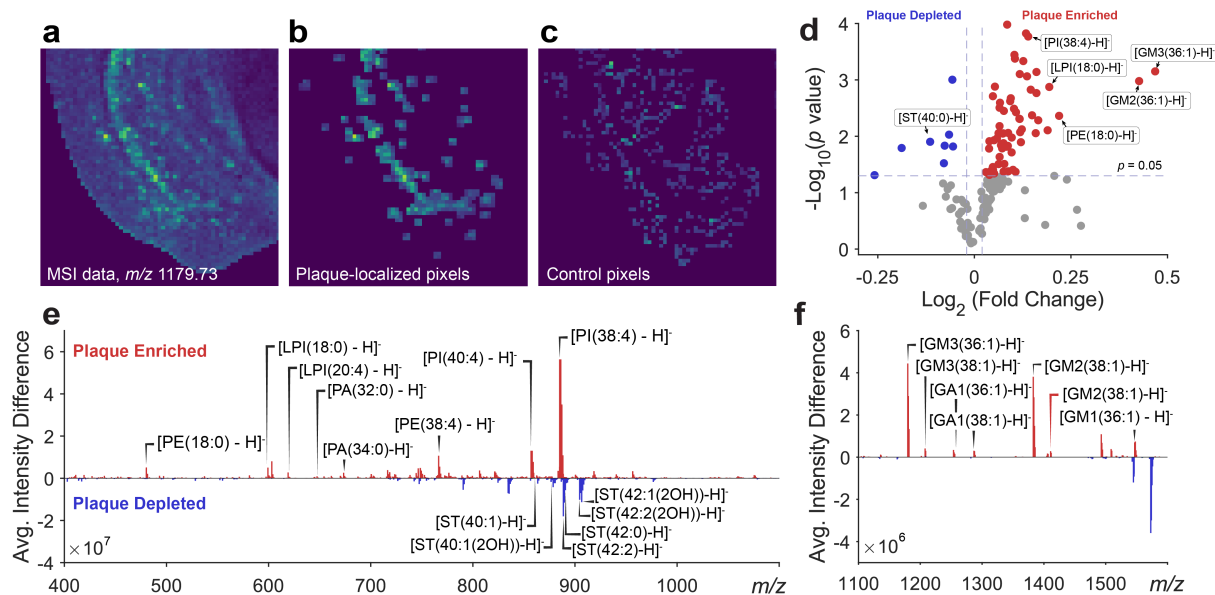

Fig 3. Non-targeted discovery of plaque-associated lipids in 5xFAD mice (*n*=3 animals, two sections per animal). **(a)** Representative ion image at *m/z* 1179.73, representative of all measurements from 5xFAD animals. **(b)** Extraction of plaque-localized pixels from the ion image **(c)** Extraction of control pixels from the same ion image **(d)** Volcano plot highlighting discovery of plaque enriched and depleted lipids **(e)** Average difference mass spectrum highlights discovered enriched and depleted lipids **(f)** A zoomed-in region of the difference plot from *m/z* 1100 to 1600 is included to highlight ganglioside differences.

phosphatidylethanolamines (PE), phosphatidylinositols (PI), and *lyso*-phosphatidylinositols (LPI). In contrast, sulfatides (ST) including oxidized sulfatides (ST(OH)) were depleted within plaques. To provide additional confidence in lipid identifications beyond mass matching, on-tissue MS/MS was obtained for selected altered lipids (Fig. S5-S7). We next sought to investigate how lipids were altered beyond the single-plaque level by investigating changes across major brain regions.

Brain-regional analysis

To contextualize the discovered plaque-associated lipids, we investigated lipid alterations across larger anatomical regions between 5xFAD and wild type (WT) animals. Specifically, we investigated the hippocampus, cerebral cortex, entorhinal cortex, and midbrain. We observed that many plaque-associated lipids also exhibited significant brain-region-wide dysregulation. For instance, LPI(18:0) was significantly enriched in 5xFAD mice relative to WT animals ($p \leq$ 0.05 via paired t-test) in the brain regions investigated except the midbrain (Fig. 4b). Similar trends were observed for other plaque-associated lipids, including GM3(36:1) and GM2(36:1 (Fig. 4c-f). Although not achieving statistical significance, sulfatides ST(42:1) and ST(42:1(2OH) show a trend of decrease across all major brain regions (Fig. 4e-f). The regions more susceptible to pathologies (e.g., hippocampus and cerebral cortex) seem to exhibit stronger lipid alterations than other regions.

We further hypothesized that plaques which appear identical in Thioflavin S-stained microscopy images may be associated with different lipids depending on the brain region in which they are located. To investigate this hypothesis, all plaque MSI pixels from 5xFAD animals (*n*=3) including all discovered plaque-associated lipids were submitted to t-SNE and labeled according to brain region (Fig. 4g). We observed brain region-dependent clustering, with the midbrain most isolated from other clusters. We further compared normalized fluorescence images to MSI data for several plaque-enriched lipids across brain regions (Fig. 4h). Specifically, the fluorescence intensity of Thioflavin S and the ion intensities in each brain region were normalized to their respective maximum values across all brain regions to enable comparison. In the hippocampus, a region that exhibits high pathology, the fluorescence intensity of Thioflavin S closely followed the lipid signal intensity for all the species studied. Notably, some differences were observed in the cerebral cortex and midbrain. For instance, the signal intensity for GM3(36:1) was much lower in the midbrain than the staining intensity would suggest, which is also the brain region where this lipid is least abundant (Fig. 4c). This observation is further highlighted by comparison of whole-coronal-slice fluorescence images to an ion image of GM3(36:1) (Fig. 4i). Although significant Thioflavin S positive plaques are found in the midbrain, GM3(36:1) is less abundant in this region relative to the other regions studied. This trend of GM3-association with plaques also follows its natural abundance in the brain in WT mice (Fig. 4c). In contrast, other lipids were plaque-associated across all brain regions. For instance, LPI(18:0) was abundant across the hippocampus, cerebral cortex, and entorhinal cortex. Taken together, these findings provide strong evidence of regional heterogeneities in the composition of lipids associated with AD pathologies.
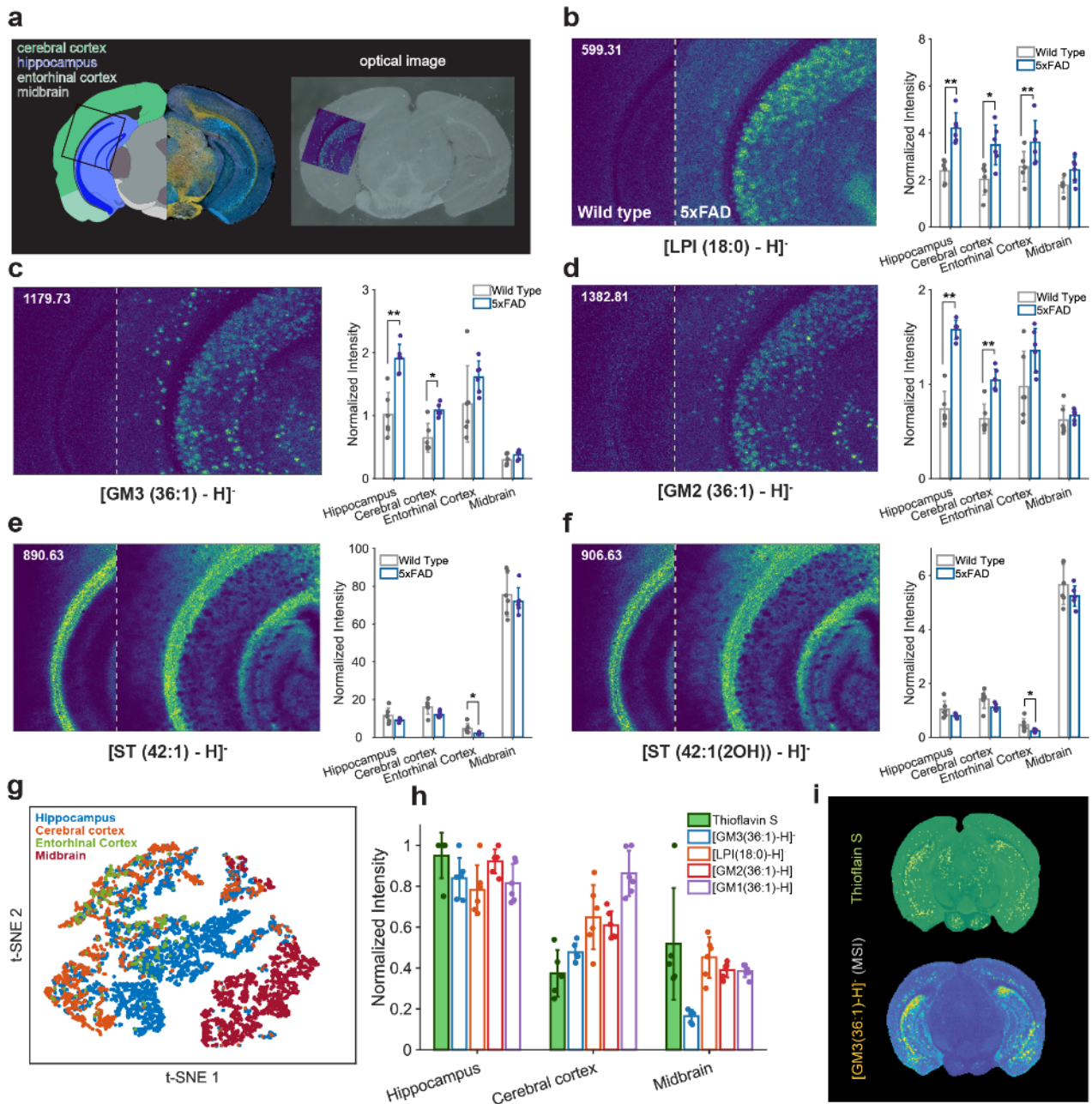
Fig 4. (a) Anatomical annotations for brain regions studied and optical image showing location region of interest (ROI) for high-spatial-resolution imaging. **(b-f)** (Left) Ion image at 5 µm spot size and pitch of plaque associated lipids and (Right) their relative amounts in various brain regions determined from whole-brain-slice imaging at 50 µm spot size and pitch (*n*=6 animals, 2 sections per animal). Error bars represent one standard deviation. **(g)** t-SNE of all plaque-localized pixels showing regional heterogeneity. **(h)** Comparison of normalized Thioflavin S intensity to normalized intensity for select plaque-associated ions. (*n*=6 animals, 2 sections per animal). Error bars represent one standard deviation. **(i)** Representative Thioflavin S staining across an entire coronal section compared (top) compared to intensity for GM3(36:1). The staining and MSI are representative of six measurements (*n*=3 5xFAD animals, two sections per animal). *$p \leq 0.05$, **$p \leq 0.01$ via paired *t*-test.

Trapped ion mobility of separation of AD-associated glycolipid isomers

Next, we enabled trapped ion mobility spectrometry (TIMS) in order to determine which plaque-associated lipids consisted of multiple isomers, and then to separate them and map their spatial distribution. We observed that GM1(36:1) and GM1(38:1) both produced two peaks with unique mobilities at the same *m/z*. Gangliosides are glycolipids composed of a ceramide chain and a glycan, and we putatively assigned the isomers as GM1a and GM1b, which differ in the position of the sialic acid, a charged sugar, on the glycan (Fig. 5a,c). Performing MSI with TIMS engaged revealed unique spatial distributions for each peak (Fig. 5). Notably, both a- and b-isomers were associated with Aβ plaques, suggesting that at least the localization of sialic acid residue within GM1 does not play a major role in its association with Aβ plaques. The differences in their localization was observed in other regions, for instance, GM1b(36:1) was more enriched in the white matter of the corpus callosum relative to GM1a(36:1) (Fig. 5b and 5d), as illustrated by the blue color in this region.

To confirm the identity of each isomer, we performed on-tissue TIMS with MS/MS (Fig. S8). Because the TIMS separation occurs prior to the collision cell, fragment ions share the mobility of their precursor, such that diagnostic fragment ions can be assigned to each mobility resolved
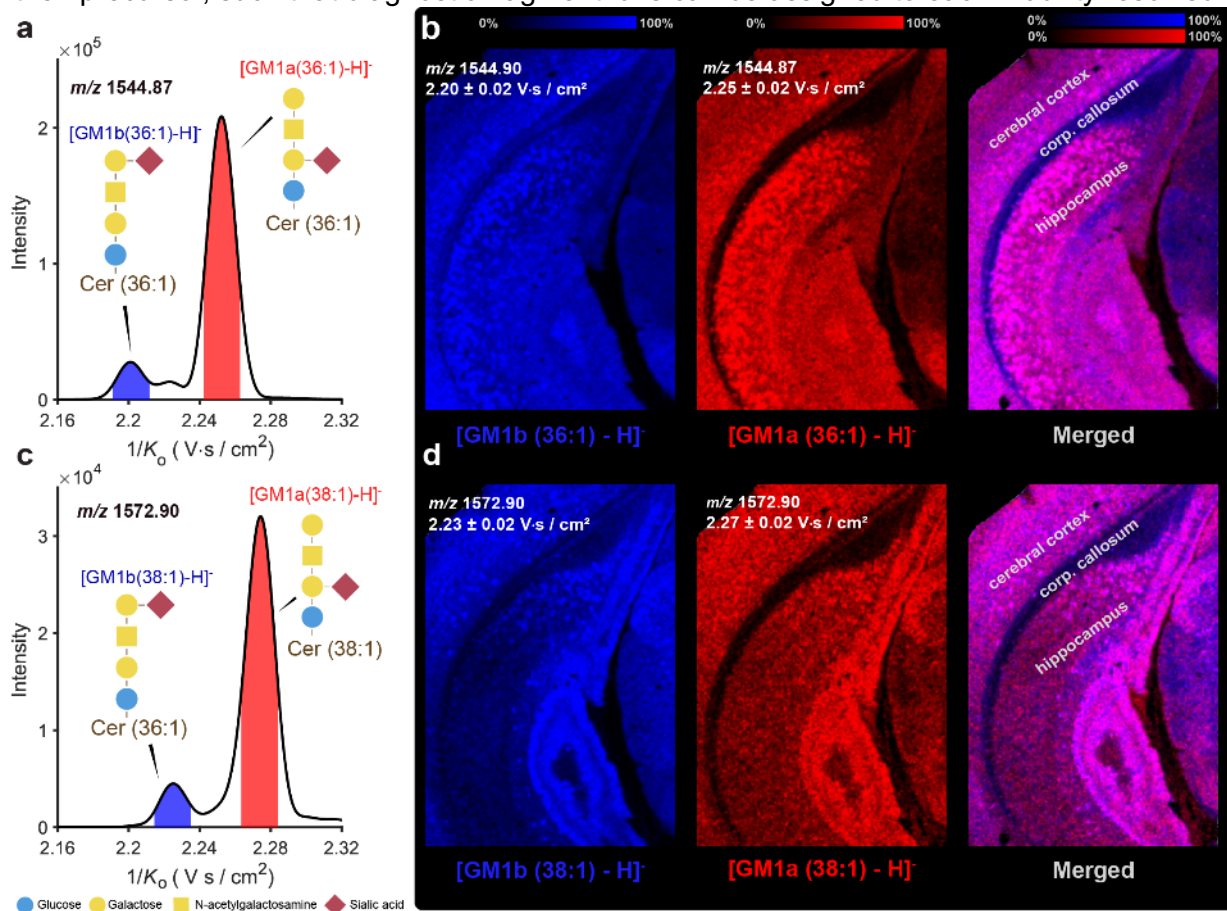

Fig 5. (a) Extracted ion mobilogram (EIM) at *m/z* 1544.87 shows the TIMS-enabled separation of GM1b(36:1) and GM1a(36:1). **(b)** Ion images are shown for mobility-selected GM1b(36:1) in blue, GM1a(36:1) in red, and a merged image of both. In **(c)** the EIM at *m/z* 1572.90 shows separation of the a- and b- isomers of a longer-chain version of GM1, GM1(38:1) with corresponding ion images in **(d)**.

peak. Based on diagnostic fragment ions, we identified the earlier eluting peak as GM1b and later eluting peak as GM1a. These results build off previous MALDI TIMS separation of ganglioside isomers,[34,35] shown here for the first time in a neurodegenerative disease model.

Discussion

We have shown that advanced MSI tools can greatly expand our understanding of biochemical alterations in Alzheimer's disease. By jointly studying plaque-associated lipids and their regional alterations, we discovered previously unseen rich heterogeneities in lipid profiles associated with individual plaques across the brain. Notably, while GM3 accumulated in plaques in the hippocampus, cerebral cortex, and entorhinal cortex, GM3 was not found in high abundance in plaques in the midbrain. This finding is interesting given the evidence that gangliosides promote the amyloidogenic processing and serve as "seeds" to promote amyloid fibrilogenesis.[36,37] Our findings suggest that ganglioside-mediated formation of Aβ plaques may occur differently across brain regions, a hypothesis which could further explored with spatial transcriptomics to provide insight into region-specific ganglioside synthesis activity.

In addition to regional variations, we demonstrated ion mobility-enabled resolution of a- and b-series ganglioside isomers. This capability may be critical to understanding Alzheimer's lipid pathology. For instance, previous work such as that Taki et al.[38] showed alterations in b-series gangliosides (e.g., GD1b and GT1b), but not in a-series gangliosides in postmortem AD tissue, suggesting they play distinct roles. However, the separation of GM1a and GM1b isomers has not previously been shown in AD tissue—an advance facilitated by our methodology. Resolving more subtle forms of isomerization, such as C=C geometry and sn-position may require the addition of derivatization, ion/ion reactions and/or ion multiplexing techniques.[39,40] Further, many of the plaque-associated lipids identified in our study, including gangliosides GM1 and GM3, also show altered concentrations in plasma[41,42] suggesting that MSI-guided findings can be used to refine lipid biomarker panels for early AD diagnosis.

Still, a key question remains: to what extent are the observed lipid accumulations due to enrichment in plasma membranes versus extracellular transport. While many plaque-associated lipids are likely to be enriched in plasma membranes, there is increasing evidence supporting lipid variation through extracellular vesicle packaging and release during AD.[43] The characterization of extracellular vesicles in AD models, combined with MSI, could provide critical insight into the mechanism of lipid transport and distribution, providing a better understanding of their role in AD pathology.

Last, we note that alterations in cell type and composition around Aβ plaques, such as accumulation of reactive astrocytes[44] and morphological changes to microglia[45] are likely contributors to the lipid heterogeneity observed. These cellular changes, along with their structural alterations, are expected to have a direct impact on the lipid profiles within Aβ plaque regions. The emerging field of single cell proteomics and metabolomics holds great potential for uncovering the cell-type specific contributions to lipid biosynthesis and distribution.[46,47] High spatial resolution MSI, supported by proteomics and immunofluorescence, offers a powerful strategy to unravel the intricate relationship between cell type and lipid alterations.

Conclusions

We introduced a novel pipeline for unbiased discovery of Aβ plaque-associated lipids and mapped them with high spatial resolution and isomer separation. This was enabled by the integration of fluorescence microscopy, MALDI-2 ion mobility / mass spectrometry, and computational tools. Our approach can be extended to achieve spatial lipidomics and

metabolomics in various disease models and tissue types. Work is ongoing to extend this approach to characterize the lipidome in other AD models and human samples.

Beyond AD, this pipeline is well suited to examining regional differences in lipids at defined locations within the brain, whether these are extracellular plaques, rare cells, or specific locations containing diseased tissue. The requirement is that these locations are highlighted via morphological or fluorescence-imaging. The incorporation of photocleavable mass-tags[48,49] is an intriguing approach to make the pipeline fully MS-compatible. Photocleavable mass tags provide multiplexed tagging, which could allow more cell types and key protein markers to be detected than traditional fluorescence microscopy. This approach can also correlate changes in cell composition to plaque morphology, allowing inference of detailed brain response to plaque formation.

Methods

Chemicals and Reagents

Thioflavin S, 2,5-dihydroxyacetophenone (DHAP), methanol, acetonitrile, ethanol, and paraformaldehyde (PFA) were purchased from Sigma Aldrich. Hoechst 33342, tris-buffered saline (TBS), and phosphate-buffered saline (PBS) were obtained from Thermo Fisher Scientific.

Animals

Five-month-old female 5xFAD mice[25] along with age- and sex- matched wild type controls (C57BL/6) were studied (*n*=3 per group). Animals were housed in a 12 h light cycle and fed ad libitum. Euthanasia of animals was conducted via slow asphyxiation using CO_2 gas following the animal use protocol approved by the Illinois Institutional Animal Care and Use Committee with strict adherence to both national and ARRIVE standards for the ethical treatment and care of animals.

Sample Preparation

Immediately after euthanasia, animals were transcardially perfused with 60 mL of ice-cold modified Gey's balanced salt solution (mGBSS).[50] Brains were quickly surgically dissected and frozen on dry ice. To obtain thin tissue sections for MSI, brain regions from all six animals were adhered onto the chuck of a cryostat-microtome (Leica Biosystems) with deionized water. Coronal sections of 12 µm thickness were obtained at bregma -2.80 ± 0.2 mm and thaw mounted onto ITO-coated glass slides (Delta Technologies, Loveland, CO). To help mitigate batch effects all animals studied were sectioned simultaneously and thaw-mounted together onto a given slide.

Tissue sections were coated with 2,5-dihydroxyacetophenone (DHAP) at 10 mg/mL in 8:1:1: MeOH:ACN:H_2O using an HTX-M5 Sprayer (HTX Technologies, Chapel Hill, NC). Matrix was applied with 10 passes using a flow rate of 125 µL/min and a nozzle temperature of 60 ˚C. The sprayer was set to a distance of 60 mm from the sample and applied at 10 psi with a velocity of 1200 mm/min. Ten passes of matrix were applied with 15 s drying time between passes.

For high-spatial-resolution tissue imaging of lipids, DHAP was applied with a laboratory fabricated sublimation setup. The setup consisted of a glass sublimation apparatus (Wilmad Glass) placed onto a heated sand bath. Briefly, ~500 mg of DHAP was evenly spread onto the bottom of the sublimation chamber using a stainless-steel tea strainer. An ITO-coated glass slide was attached to the bottom of the cold finger with double-sided copper tape and sealed within the apparatus with an O-Ring. Vacuum was established using a rough pump. The cold finger was then filled with an ice-water slush. Matrix was sublimed by placing the apparatus onto a sand bath heated to 170 °C for 2 min applying a matrix density of 50 µg/cm^2.

For TIMS imaging, DHAP matrix was applied with a newly acquired HTX SubliMATE (HTX Technologies) by aliquoting 40 mg of matrix into the ceramic wafer. Next, vacuum pressure was stabilized to ca. 40 mtorr while the top of the apparatus was cooled with an ice-water slush for 5 min. Matrix was sublimed by heating the ceramic wafer to 200 °C for 5 min, yielding a matrix density of 120 µg/cm^2.

Mass spectrometry imaging

Lipid MSI was performed on a timsTOF fleX MALDI-2 trapped ion mobility quadrupole time-of-flight mass spectrometer (Bruker Corp., Billerica, MA).The instrument was equipped with a Bruker SmartBeam 3D Laser consisting of two Nd:YAG lasers operating at 355 nm (frequency tripled) and 266 nm (frequency quadrupled) for MALDI and MALDI-2, respectively. The instrument was configured and controlled using timsControl (Client version 5.1.2) and flexImaging (Version 7.4, Bruker Daltonics GmbH & Co. KG). Detailed instrument settings are provided in Table S1. For high spatial-resolution imaging, tissue sections with sublimed matrix application were imaged using a "Single M2" beam with either a 5×5 μm^2 (TIMS off) or 10×10 μm^2 (TIMS on) spot size. To profile global changes, two tissue sections from each animal (n=6 animals, n=12 sections) were imaged with the "M5 M2" laser beam generating a 50×50 μm^2 spot size. Spectra were collected at 1 kHz with 100 shots and a post-ionization delay of 10 µs. Before every acquisition, mass calibration was performed using red phosphorus in LDI mode. Lock mass calibration was performed using three abundant lipid ions.

Trapped ion mobility imaging

TIMS with high resolving power was performed to resolve ganglioside isomers using a 25 ms accumulation time with a 1400 ms ramp time. The TIMS In N_2 pressure was increased to ~2.55 mbar in order to increase the resolution for high m/z ions.[51] Concurrently, the Δt6 (Ramp Start -> Accumulation Exit) voltage was increased to -175 V to access higher mobilities. A detailed set of TIMS parameters are provided in Table S2. Mobility calibration was performed using the ESI source with ESI-L low concentration tuning mix (Agilent Technologies, USA).

Post-MALDI Histological staining

To correlate lipid distributions with amyloid plaque accumulation, the same brain sections analyzed by MSI were subsequently stained with Thioflavin S based on previous protocols[52] and modified for MSI. First, DHAP matrix was removed by washing sections in 50% EtOH for 5 min. Next, tissues were fixed in 4% PFA in 1x PBS for 20 min. After fixation, sections were washed for 2 min in 1x in TBS with 0.1% Tween 20 (TBST), followed by a quick wash in TBS and then incubated with 1% w/w Thioflavin S, filtered by 22 µm, for 8 min in the dark. After amyloid staining, sections were washed with 80% EtOH (2x for 3 min), 95 % EtOH (3 min) and then stained for nuclei in Hoechst 33342 (0.5 µg/mL in 1x TBS) for 10 min. Slides were briefly dried under N_2 and mounted with ProlongGold™ Antifade. Tiled fluorescence images were obtained on an Axio M2 imager (Zeiss, Jena, Germany) equipped with an AxioCam ICc5 camera and a .63× camera adaptor and an X-cite Series 120 Q mercury lamp (Lumen Dynamics, Mississauga, Canada). Images were obtained with a 10x air objective with 20% tile overlap using GFP (ex. 450–490 nm; em. 500–550 nm) and DAPI (ex. 335–383 nm; em. 420–470 nm) filter cubes for Thioflavin S and Hoechst, respectively. Images were exported as .jpeg files for downstream processing.

Data analysis

Raw binary Bruker .d data files were parsed into Python using pyTDF-SDK.[53] Peak picking was performed on an average spectrum generated from all pixels from each imaging file. After peak picking, data were aligned to a common set of m/z vales. Data were subsequently written as .mat files for processing MATLAB 2022b. Coregistration of fluorescence and MSI data was performed using affine transformation with at least 8 support points in each of the images. Anatomical annotation was performed by manually drawing regions of interest with reference to the Allen Brain Atlas.[54] Plaque-positive pixels from each of the regions were submitted to t-SNE for unsupervised clustering. Each pixel consisted of an array of m/z values for all discovered plaque-associated lipids.

Statistical analysis

Data were checked for normality using a Shapiro Wilk test. Suitably normal data (p>0.05 from Shapiro Wilk) were compared with a two-tailed t-test. t-SNE was performed in MATLAB 2022b with the function 't-sne' using Euclidean distance as the distance metric and with all other parameters as default.

Code Availability

The scripts used to perform image registration and regional analysis are publicly available on GitHub at https://github.com/timtk1/MALDI2Alz.

Data Availability

The data that support the findings of this study are publicly available via the Illinois Data Bank (https://doi.org/10.13012/B2IDB-4907703_V1)

Acknowledgements

Author Contributions

T.J.T., J.V.S., F.L., and O.L. conceptualized the project. O.L. and S.R. provided animals. S.S. prepared the animal samples. T.J.T. and. S.C. wrote the code for data analysis. T.J.T. and S.O. performed mass spectrometry imaging. T.J.T and M.A. performed fluorescence microscopy. T.J.T. wrote an initial draft of the manuscript. T.J.T., J.V.S., F.L., and O.L. contributed to editing the manuscript. All authors contributed to the discussion of the project and have reviewed and approved the final paper.

Supporting Information

MALDI-TOF imaging of Aβ peptides and comparison to Thioflavin S staining. Detailed instrumental parameters for MALDI imaging and TIMS. Comparison of MALDI-1 to MALDI-2 signal intensity for AD-associated lipids. MS/MS spectra of putatively discovered lipids. TIMS-CID of GM1a and GM1b.

References

(1)   Masters, C. L.; Bateman, R.; Blennow, K.; Rowe, C. C.; Sperling, R. A.; Cummings, J. L. Alzheimer's Disease. *Nat. Rev. Dis. Primer* **2015**, *1* (1), 15056. https://doi.org/10.1038/nrdp.2015.56.

(2)   Long, J. M.; Holtzman, D. M. Alzheimer Disease: An Update on Pathobiology and Treatment Strategies. *Cell* **2019**, *179* (2), 312–339. https://doi.org/10.1016/j.cell.2019.09.001.

(3)   Chen, W.-T.; Lu, A.; Craessaerts, K.; Pavie, B.; Sala Frigerio, C.; Corthout, N.; Qian, X.; Laláková, J.; Kühnemund, M.; Voytyuk, I.; Wolfs, L.; Mancuso, R.; Salta, E.; Balusu, S.; Snellinx, A.; Munck, S.; Jurek, A.; Fernandez Navarro, J.; Saido, T. C.; Huitinga, I.; Lundeberg, J.; Fiers, M.; De Strooper, B. Spatial Transcriptomics and In Situ Sequencing to Study Alzheimer's Disease. *Cell* **2020**, *182* (4), 976-991.e19. https://doi.org/10.1016/j.cell.2020.06.038.

(4)   Wong, M. W.; Braidy, N.; Poljak, A.; Pickford, R.; Thambisetty, M.; Sachdev, P. S. Dysregulation of Lipids in Alzheimer's Disease and Their Role as Potential Biomarkers. *Alzheimers Dement.* **2017**, *13* (7), 810–827. https://doi.org/10.1016/j.jalz.2017.01.008.

(5)   Martens, Y. A.; Zhao, N.; Liu, C.-C.; Kanekiyo, T.; Yang, A. J.; Goate, A. M.; Holtzman, D. M.; Bu, G. ApoE Cascade Hypothesis in the Pathogenesis of Alzheimer's Disease and Related Dementias. *Neuron* **2022**, *110* (8), 1304–1317. https://doi.org/10.1016/j.neuron.2022.03.004.

(6)   Candore, G.; Bulati, M.; Caruso, C.; Castiglia, L.; Colonna-Romano, G.; Di Bona, D.; Duro, G.; Lio, D.; Matranga, D.; Pellicanò, M.; Rizzo, C.; Scapagnini, G.; Vasto, S. Inflammation, Cytokines, Immune Response, Apolipoprotein E, Cholesterol, and Oxidative Stress in Alzheimer Disease: Therapeutic Implications. *Rejuvenation Res.* **2010**, *13* (2–3), 301–313. https://doi.org/10.1089/rej.2009.0993.

(7)   Cheng, H.; Vetrivel, K. S.; Gong, P.; Meckler, X.; Parent, A.; Thinakaran, G. Mechanisms of Disease: New Therapeutic Strategies for Alzheimer's Disease—Targeting APP Processing in Lipid Rafts. *Nat. Clin. Pract. Neurol.* **2007**, *3* (7), 374–382. https://doi.org/10.1038/ncpneuro0549.

(8)   Han, X. Potential Mechanisms Contributing to Sulfatide Depletion at the Earliest Clinically Recognizable Stage of Alzheimer's Disease: A Tale of Shotgun Lipidomics. *J. Neurochem.* **2007**, *103* (s1), 171–179. https://doi.org/10.1111/j.1471-4159.2007.04708.x.

(9) Gode, D.; Volmer, D. A. Lipid Imaging by Mass Spectrometry – a Review. *The Analyst* **2013**, *138* (5), 1289. https://doi.org/10.1039/c2an36337b.

(10) Xie, Y. R.; Castro, D. C.; Rubakhin, S. S.; Trinklein, T. J.; Sweedler, J. V.; Lam, F. Multiscale Biochemical Mapping of the Brain through Deep-Learning-Enhanced High-Throughput Mass Spectrometry. *Nat. Methods* **2024**. https://doi.org/10.1038/s41592-024-02171-3.

(11) Seth W Croslow; Timothy J Trinklein; Jonathan V Sweedler. Advances in Multimodal Mass Spectrometry for Single-Cell Analysis and Imaging Enhancement. *FEBS Lett. 598*, 591–601. https://doi.org/doi:10.1002/1873-3468.14798.

(12) Carlred, L.; Michno, W.; Kaya, I.; Sjövall, P.; Syvänen, S.; Hanrieder, J. Probing Amyloid-β Pathology in Transgenic Alzheimer's Disease (tgArcSwe) Mice Using MALDI Imaging Mass Spectrometry. *J. Neurochem.* **2016**, *138* (3), 469–478. https://doi.org/10.1111/jnc.13645.

(13) Kaya, I.; Brinet, D.; Michno, W.; Syvänen, S.; Sehlin, D.; Zetterberg, H.; Blennow, K.; Hanrieder, J. Delineating Amyloid Plaque Associated Neuronal Sphingolipids in Transgenic Alzheimer's Disease Mice (tgArcSwe) Using MALDI Imaging Mass Spectrometry. *ACS Chem. Neurosci.* **2017**, *8* (2), 347–355. https://doi.org/10.1021/acschemneuro.6b00391.

(14) Kaya, I.; Brinet, D.; Michno, W.; Başkurt, M.; Zetterberg, H.; Blenow, K.; Hanrieder, J. Novel Trimodal MALDI Imaging Mass Spectrometry (IMS3) at 10 Mm Reveals Spatial Lipid and Peptide Correlates Implicated in Aβ Plaque Pathology in Alzheimer's Disease. *ACS Chem. Neurosci.* **2017**, *8* (12), 2778–2790. https://doi.org/10.1021/acschemneuro.7b00314.

(15) Kaya, I.; Zetterberg, H.; Blennow, K.; Hanrieder, J. Shedding Light on the Molecular Pathology of Amyloid Plaques in Transgenic Alzheimer's Disease Mice Using Multimodal MALDI Imaging Mass Spectrometry. *ACS Chem. Neurosci.* **2018**, *9* (7), 1802–1817. https://doi.org/10.1021/acschemneuro.8b00121.

(16) Ge, J.; Koutarapu, S.; Jha, D.; Dulewicz, M.; Zetterberg, H.; Blennow, K.; Hanrieder, J. Tetramodal Chemical Imaging Delineates the Lipid–Amyloid Peptide Interplay at Single Plaques in Transgenic Alzheimer's Disease Models. *Anal. Chem.* **2023**, *95* (10), 4692–4702. https://doi.org/10.1021/acs.analchem.2c05302.

(17) Stoeckli, M.; Staab, D.; Staufenbiel, M.; Wiederhold, K.-H.; Signor, L. Molecular Imaging of Amyloid b Peptides in Mouse Brain Sections Using Mass Spectrometry. *Anal. Biochem.* **2002**.

(18) Hong, J. H.; Kang, J. W.; Kim, D. K.; Baik, S. H.; Kim, K. H.; Shanta, S. R.; Jung, J. H.; Mook-Jung, I.; Kim, K. P. Global Changes of Phospholipids Identified by MALDI Imaging Mass Spectrometry in a Mouse Model of Alzheimer's Disease. *J. Lipid Res.* **2016**, *57* (1), 36–45. https://doi.org/10.1194/jlr.M057869.

(19) Ollen-Bittle, N.; Pejhan, S.; Pasternak, S. H.; Keene, C. D.; Zhang, Q.; Whitehead, S. N. Co-Registration of MALDI-MSI and Histology Demonstrates Gangliosides Co-Localize with Amyloid Beta Plaques in Alzheimer's Disease. *Acta Neuropathol. (Berl.)* **2024**, *147* (1), 105. https://doi.org/10.1007/s00401-024-02759-1.

(20) Caughlin, S.; Maheshwari, S.; Agca, Y.; Agca, C.; Harris, A. J.; Jurcic, K.; Yeung, K. K.-C.; Cechetto, D. F.; Whitehead, S. N. Membrane-Lipid Homeostasis in a Prodromal Rat Model of Alzheimer's Disease: Characteristic Profiles in Ganglioside Distributions during Aging Detected Using MALDI Imaging Mass Spectrometry. *Biochim. Biophys. Acta BBA - Gen. Subj.* **2018**, *1862* (6), 1327–1338. https://doi.org/10.1016/j.bbagen.2018.03.011.

(21) Michno, W.; Bowman, A.; Jha, D.; Minta, K.; Ge, J.; Koutarapu, S.; Zetterberg, H.; Blennow, K.; Lashley, T.; Heeren, R. M. A.; Hanrieder, J. Spatial Neurolipidomics at the Single Amyloid-β Plaque Level in Postmortem Human Alzheimer's Disease Brain. *ACS Chem. Neurosci.* **2024**, *15* (4), 877–888. https://doi.org/10.1021/acschemneuro.4c00006.

(22) Mendis, L. H. S.; Grey, A. C.; Faull, R. L. M.; Curtis, M. A. Hippocampal Lipid Differences in Alzheimer's Disease: A Human Brain Study Using Matrix-assisted Laser Desorption/Ionization-imaging Mass Spectrometry. *Brain Behav.* **2016**, *6* (10), e00517. https://doi.org/10.1002/brb3.517.

(23) Kakuda, N.; Miyasaka, T.; Iwasaki, N.; Nirasawa, T.; Wada-Kakuda, S.; Takahashi-Fujigasaki, J.; Murayama, S.; Ihara, Y.; Ikegawa, M. Distinct Deposition of Amyloid-β Species in Brains with Alzheimer's Disease Pathology Visualized with MALDI Imaging Mass Spectrometry. *Acta Neuropathol. Commun.* **2017**, *5* (1), 73. https://doi.org/10.1186/s40478-017-0477-x.

(24) Enzlein, T.; Lashley, T.; Sammour, D. A.; Hopf, C.; Chávez-Gutiérrez, L. Integrative Single-Plaque Analysis Reveals Signature Aβ and Lipid Profiles in the Alzheimer's Brain. *Anal. Chem.* **2024**, acs.analchem.3c05557. https://doi.org/10.1021/acs.analchem.3c05557.

(25) Oakley, H.; Cole, S. L.; Logan, S.; Maus, E.; Shao, P.; Craft, J.; Guillozet-Bongaarts, A.; Ohno, M.; Disterhoft, J.; Van Eldik, L.; Berry, R.; Vassar, R. Intraneuronal β-Amyloid Aggregates, Neurodegeneration, and Neuron Loss in Transgenic Mice with Five Familial Alzheimer's Disease Mutations: Potential Factors in Amyloid Plaque Formation. *J. Neurosci.* **2006**, *26* (40), 10129–10140. https://doi.org/10.1523/JNEUROSCI.1202-06.2006.

(26) Mishra, R.; Phan, T.; Kumar, P.; Morrissey, Z.; Gupta, M.; Hollands, C.; Shetti, A.; Lopez, K. L.; Maienschein-Cline, M.; Suh, H.; Hen, R.; Lazarov, O. Augmenting Neurogenesis Rescues Memory Impairments in Alzheimer's Disease by Restoring the Memory-Storing Neurons. *J. Exp. Med.* **2022**, *219* (9), e20220391. https://doi.org/10.1084/jem.20220391.

(27) Soltwisch, J.; Kettling, H.; Vens-Cappell, S.; Wiegelmann, M.; Müthing, J.; Dreisewerd, K. Mass Spectrometry Imaging with Laser-Induced Postionization. *Science* **2015**, *348* (6231), 211–215. https://doi.org/10.1126/science.aaa1051.

(28) Niehaus, M.; Soltwisch, J.; Belov, M. E.; Dreisewerd, K. Transmission-Mode MALDI-2 Mass Spectrometry Imaging of Cells and Tissues at Subcellular Resolution. *Nat. Methods* **2019**, *16* (9), 925–931. https://doi.org/10.1038/s41592-019-0536-2.

(29) Comi, T. J.; Neumann, E. K.; Do, T. D.; Sweedler, J. V. microMS: A Python Platform for Image-Guided Mass Spectrometry Profiling. *J. Am. Soc. Mass Spectrom.* **2017**, *28* (9), 1919–1928. https://doi.org/10.1007/s13361-017-1704-1.

(30) Neumann, E. K.; Ellis, J. F.; Triplett, A. E.; Rubakhin, S. S.; Sweedler, J. V. Lipid Analysis of 30 000 Individual Rodent Cerebellar Cells Using High-Resolution Mass Spectrometry. *Anal. Chem.* **2019**, *91* (12), 7871–7878. https://doi.org/10.1021/acs.analchem.9b01689.

(31) Castro, D. C.; Xie, Y. R.; Rubakhin, S. S.; Romanova, E. V.; Sweedler, J. V. Image-Guided MALDI Mass Spectrometry for High-Throughput Single-Organelle Characterization. *Nat. Methods* **2021**, *18* (10), 1233–1238. https://doi.org/10.1038/s41592-021-01277-2.

(32) Kaya, I.; Jennische, E.; Dunevall, J.; Lange, S.; Ewing, A. G.; Malmberg, P.; Baykal, A. T.; Fletcher, J. S. Spatial Lipidomics Reveals Region and Long Chain Base Specific Accumulations of Monosialogangliosides in Amyloid Plaques in Familial Alzheimer's Disease Mice (5xFAD) Brain. *ACS Chem. Neurosci.* **2020**, *11* (1), 14–24. https://doi.org/10.1021/acschemneuro.9b00532.

(33) Conroy, M. J.; Andrews, R. M.; Andrews, S.; Cockayne, L.; Dennis, E. A.; Fahy, E.; Gaud, C.; Griffiths, W. J.; Jukes, G.; Kolchin, M.; Mendivelso, K.; Lopez-Clavijo, A. F.; Ready, C.; Subramaniam, S.; O'Donnell, V. B. LIPID MAPS: Update to Databases and Tools for the Lipidomics Community. *Nucleic Acids Res.* **2024**, *52* (D1), D1677–D1682. https://doi.org/10.1093/nar/gkad896.

(34) Djambazova, K. V.; Dufresne, M.; Migas, L. G.; Kruse, A. R. S.; Van De Plas, R.; Caprioli, R. M.; Spraggins, J. M. MALDI TIMS IMS of Disialoganglioside Isomers–GD1a and GD1b in Murine Brain Tissue. *Anal. Chem.* **2022**, acs.analchem.2c03939. https://doi.org/10.1021/acs.analchem.2c03939.

(35) Djambazova, K. V.; Gibson-Corley, K. N.; Freiberg, J. A.; Caprioli, R. M.; Skaar, E. P.; Spraggins, J. M. MALDI TIMS IMS Reveals Ganglioside Molecular Diversity within Murine *S. Aureus* Kidney Tissue

Abscesses. *J. Am. Soc. Mass Spectrom.* **2024**, *35* (8), 1692–1701. https://doi.org/10.1021/jasms.4c00089.

(36) Dodge, J. C.; Tamsett, T. J.; Treleaven, C. M.; Taksir, T. V.; Piepenhagen, P.; Sardi, S. P.; Cheng, S. H.; Shihabuddin, L. S. Glucosylceramide Synthase Inhibition Reduces Ganglioside GM3 Accumulation, Alleviates Amyloid Neuropathology, and Stabilizes Remote Contextual Memory in a Mouse Model of Alzheimer's Disease. *Alzheimers Res. Ther.* **2022**, *14* (1), 19. https://doi.org/10.1186/s13195-022-00966-0.

(37) Kakio, A.; Nishimoto, S.; Yanagisawa, K.; Kozutsumi, Y.; Matsuzaki, K. Interactions of Amyloid β-Protein with Various Gangliosides in Raft-Like Membranes: Importance of GM1 Ganglioside-Bound Form as an Endogenous Seed for Alzheimer Amyloid. *Biochemistry* **2002**, *41* (23), 7385–7390. https://doi.org/10.1021/bi0255874.

(38) Taki, T. An Approach to Glycobiology from Glycolipidomics: Ganglioside Molecular Scanning in the Brains of Patients with Alzheimer's Disease by TLC-Blot/Matrix Assisted Laser Desorption/Ionization-Time of Flight MS. *Biol. Pharm. Bull.* **2012**, *35* (10), 1642–1647. https://doi.org/10.1248/bpb.b12-00400.

(39) Bonney, J. R.; Kang, W.-Y.; Specker, J. T.; Liang, Z.; Scoggins, T. R.; Prentice, B. M. Relative Quantification of Lipid Isomers in Imaging Mass Spectrometry Using Gas-Phase Charge Inversion Ion/Ion Reactions and Infrared Multiphoton Dissociation. *Anal. Chem.* **2023**, *95* (48), 17766–17775. https://doi.org/10.1021/acs.analchem.3c03804.

(40) Xu, S.; Zhu, Z.; Delafield, D. G.; Rigby, M. J.; Lu, G.; Braun, M.; Puglielli, L.; Li, L. Spatially and Temporally Probing Distinctive Glycerophospholipid Alterations in Alzheimer's Disease Mouse Brain via High-Resolution Ion Mobility-Enabled Sn-Position Resolved Lipidomics. *Nat. Commun.* **2024**, *15* (1), 6252. https://doi.org/10.1038/s41467-024-50299-9.

(41) Liu, L.; Zhang, K.; Tan, L.; Chen, Y.-H.; Cao, Y.-P. Alterations in Cholesterol and Ganglioside GM1 Content of Lipid Rafts in Platelets From Patients With Alzheimer Disease. *Alzheimer Dis. Assoc. Disord.* **2015**, *29* (1), 63–69. https://doi.org/10.1097/WAD.0000000000000041.

(42) Chua, X. Y.; Torta, F.; Chong, J. R.; Venketasubramanian, N.; Hilal, S.; Wenk, M. R.; Chen, C. P.; Arumugam, T. V.; Herr, D. R.; Lai, M. K. P. Lipidomics Profiling Reveals Distinct Patterns of Plasma Sphingolipid Alterations in Alzheimer's Disease and Vascular Dementia. *Alzheimers Res. Ther.* **2023**, *15* (1), 214. https://doi.org/10.1186/s13195-023-01359-7.

(43) Su, H.; Rustam, Y. H.; Masters, C. L.; Makalic, E.; McLean, C. A.; Hill, A. F.; Barnham, K. J.; Reid, G. E.; Vella, L. J. Characterization of Brain-derived Extracellular Vesicle Lipids in Alzheimer's Disease. *J. Extracell. Vesicles* **2021**, *10* (7), e12089. https://doi.org/10.1002/jev2.12089.

(44) Pike, C. J.; Cummings, B. J.; Cotman, C. W. Early Association of Reactive Astrocytes with Senile Plaques in Alzheimer's Disease. *Exp. Neurol.* **1995**, *132* (2), 172–179. https://doi.org/10.1016/0014-4886(95)90022-5.

(45) Mattiace, L. A.; Davies, P.; Yen, S.-H.; Dickson, D. W. Microglia in Cerebellar Plaques in Alzheimer's Disease. *Acta Neuropathol. (Berl.)* **1990**, *80* (5), 493–498. https://doi.org/10.1007/BF00294609.

(46) Ghatak, S.; Diedrich, J. K.; Talantova, M.; Bhadra, N.; Scott, H.; Sharma, M.; Albertolle, M.; Schork, N. J.; Yates, J. R.; Lipton, S. A. Single-Cell Patch-Clamp/Proteomics of Human Alzheimer's Disease iPSC-Derived Excitatory Neurons Versus Isogenic Wild-Type Controls Suggests Novel Causation and Therapeutic Targets. *Adv. Sci.* **2024**, *11* (29), 2400545. https://doi.org/10.1002/advs.202400545.

(47) Savas, J. N.; Wang, Y.-Z.; DeNardo, L. A.; Martinez-Bartolome, S.; McClatchy, D. B.; Hark, T. J.; Shanks, N. F.; Cozzolino, K. A.; Lavallée-Adam, M.; Smukowski, S. N.; Park, S. K.; Kelly, J. W.; Koo, E. H.; Nakagawa, T.; Masliah, E.; Ghosh, A.; Yates, J. R. Amyloid Accumulation Drives Proteome-Wide Alterations in Mouse Models of Alzheimer's Disease-like Pathology. *Cell Rep.* **2017**, *21* (9), 2614–2627. https://doi.org/10.1016/j.celrep.2017.11.009.

(48) Yagnik, G.; Liu, Z.; Rothschild, K. J.; Lim, M. J. Highly Multiplexed Immunohistochemical MALDI-MS Imaging of Biomarkers in Tissues. *J. Am. Soc. Mass Spectrom.* **2021**, *32* (4), 977–988. https://doi.org/10.1021/jasms.0c00473.

(49) Claes, B. S. R.; Krestensen, K. K.; Yagnik, G.; Grgic, A.; Kuik, C.; Lim, M. J.; Rothschild, K. J.; Vandenbosch, M.; Heeren, R. M. A. MALDI-IHC-Guided In-Depth Spatial Proteomics: Targeted and Untargeted MSI Combined. *Anal. Chem.* **2023**, *95* (4), 2329–2338. https://doi.org/10.1021/acs.analchem.2c04220.

(50) Nemes, P.; Rubakhin, S. S.; Aerts, J. T.; Sweedler, J. V. Qualitative and Quantitative Metabolomic Investigation of Single Neurons by Capillary Electrophoresis Electrospray Ionization Mass Spectrometry. *Nat. Protoc.* **2013**, *8* (4), 783–799. https://doi.org/10.1038/nprot.2013.035.

(51) Silveira, J. A.; Ridgeway, M. E.; Park, M. A. High Resolution Trapped Ion Mobility Spectrometery of Peptides. *Anal. Chem.* **2014**, *86* (12), 5624–5627. https://doi.org/10.1021/ac501261h.

(52) Lazarov, O.; Robinson, J.; Tang, Y.-P.; Hairston, I. S.; Korade-Mirnics, Z.; Lee, V. M.-Y.; Hersh, L. B.; Sapolsky, R. M.; Mirnics, K.; Sisodia, S. S. Environmental Enrichment Reduces Aβ Levels and Amyloid Deposition in Transgenic Mice. *Cell* **2005**, *120* (5), 701–713. https://doi.org/10.1016/j.cell.2005.01.015.

(53) Luu, G. T.; Freitas, M. A.; Lizama-Chamu, I.; McCaughey, C. S.; Sanchez, L. M.; Wang, M. TIMSCONVERT: A Workflow to Convert Trapped Ion Mobility Data to Open Data Formats. *Bioinformatics* **2022**, *38* (16), 4046–4047. https://doi.org/10.1093/bioinformatics/btac419.

(54) Lein, E. S.; Hawrylycz, M. J.; Ao, N.; Ayres, M.; Bensinger, A.; Bernard, A.; Boe, A. F.; Boguski, M. S.; Brockway, K. S.; Byrnes, E. J.; Chen, L.; Chen, L.; Chen, T.-M.; Chi Chin, M.; Chong, J.; Crook, B. E.; Czaplinska, A.; Dang, C. N.; Datta, S.; Dee, N. R.; Desaki, A. L.; Desta, T.; Diep, E.; Dolbeare, T. A.; Donelan, M. J.; Dong, H.-W.; Dougherty, J. G.; Duncan, B. J.; Ebbert, A. J.; Eichele, G.; Estin, L. K.; Faber, C.; Facer, B. A.; Fields, R.; Fischer, S. R.; Fliss, T. P.; Frensley, C.; Gates, S. N.; Glattfelder, K. J.; Halverson, K. R.; Hart, M. R.; Hohmann, J. G.; Howell, M. P.; Jeung, D. P.; Johnson, R. A.; Karr, P. T.; Kawal, R.; Kidney, J. M.; Knapik, R. H.; Kuan, C. L.; Lake, J. H.; Laramee, A. R.; Larsen, K. D.; Lau, C.; Lemon, T. A.; Liang, A. J.; Liu, Y.; Luong, L. T.; Michaels, J.; Morgan, J. J.; Morgan, R. J.; Mortrud, M. T.; Mosqueda, N. F.; Ng, L. L.; Ng, R.; Orta, G. J.; Overly, C. C.; Pak, T. H.; Parry, S. E.; Pathak, S. D.; Pearson, O. C.; Puchalski, R. B.; Riley, Z. L.; Rockett, H. R.; Rowland, S. A.; Royall, J. J.; Ruiz, M. J.; Sarno, N. R.; Schaffnit, K.; Shapovalova, N. V.; Sivisay, T.; Slaughterbeck, C. R.; Smith, S. C.; Smith, K. A.; Smith, B. I.; Sodt, A. J.; Stewart, N. N.; Stumpf, K.-R.; Sunkin, S. M.; Sutram, M.; Tam, A.; Teemer, C. D.; Thaller, C.; Thompson, C. L.; Varnam, L. R.; Visel, A.; Whitlock, R. M.; Wohnoutka, P. E.; Wolkey, C. K.; Wong, V. Y.; Wood, M.; Yaylaoglu, M. B.; Young, R. C.; Youngstrom, B. L.; Feng Yuan, X.; Zhang, B.; Zwingman, T. A.; Jones, A. R. Genome-Wide Atlas of Gene Expression in the Adult Mouse Brain. *Nature* **2007**, *445* (7124), 168–176. https://doi.org/10.1038/nature05453.